Evaluation of a new snow albedo scheme for the Greenland ice sheet in the regional climate model RACMO2

Christiaan T. van Dalum[1], Willem Jan van de Berg[1], Stef Lhermitte[2], and Michiel R. van den Broeke[1]

[1]Institute for Marine and Atmospheric Research, Utrecht University, Utrecht, The Netherlands
[2]Department of Geoscience & Remote Sensing, Delft University of Technology, Delft, The Netherlands

Correspondence: Christiaan van Dalum (c.t.vandalum@uu.nl)

Abstract. Snow and ice albedo schemes in present day climate models often lack a sophisticated radiation penetration scheme and do not explicitly include spectral albedo variations. In this study, we evaluate a new snow albedo scheme in the regional climate model RACMO2 for the Greenland ice sheet, version 2.3p3, that includes these processes. The new albedo scheme uses the two-stream radiative transfer in snow model TARTES and the spectral-to-narrowband albedo module SNOWBAL, version 1.2. Additionally, the bare ice albedo parameterization has been updated. The snow and ice broadband and narrowband albedo output of the updated version of RACMO2 is evaluated using PROMICE and K-transect in-situ data and MODIS remote-sensing observations. Generally, the modeled narrowband and broadband albedo is in very good agreement with satellite observations, leading to a negligible domain-averaged broadband albedo bias smaller than 0.001 for the interior. Some discrepancies are, however, observed close to the ice margin. Compared to the previous model version, RACMO2.3p2, the broadband albedo is considerably higher in the bare ice zone during the ablation season, as atmospheric conditions now alter the bare ice broadband albedo. For most other regions, however, the updated broadband albedo is lower due to spectral effects, radiation penetration or enhanced snow metamorphism.

1 Introduction

The absorption of shortwave radiation is an important component of the surface energy balance of snow-covered surfaces (Van den Broeke et al., 2005; He et al., 2018b; Warren, 2019). A drop in the surface reflectivity for solar radiation, i.e., albedo, leads to more absorbed energy in the snowpack, which in turn leads to higher snow temperatures or melt. This melt-albedo feedback is initiated once snow starts to melt and the snow structure is altered, lowering the albedo (Van As et al., 2013; Jakobs et al., 2019). It is therefore imperative for regional and global climate models (RCMs and GCMs, respectively) to capture snow albedo correctly in order to reproduce the current climate and to make future climate projections for snow covered glaciated regions such as the Greenland ice sheet (GrIS).

The albedo of snow and ice is highly spectrally dependent and also depends on various other quantities. For clean snow, the spectral albedo, i.e. the albedo as a function of wavelength, is almost one for near-ultraviolet (near-UV, 300-400 nm) and visible light (400-750 nm), but drops for near-infrared (near-IR, 750-1400 nm) and is low and fluctuating for infrared (IR) radiation (Fig. 1d, Warren and Wiscombe (1980); Warren et al. (2006); Gardner and Sharp (2010); Dang et al. (2015); Picard et al.

25 (2016)). Impurities like soot and dust lower the spectral albedo significantly in the near-UV and visible part of the spectrum
(Hansen and Nazarenko, 2004; Doherty et al., 2010; Dumont et al., 2014; Tuzet et al., 2017). Snow metamorphism, which
leads to increased snow density and grain radius, alters the albedo as well, especially for the (near-)IR radiation (Wyser and
Yang, 1998; King et al., 2004; Tuzet et al., 2019; He and Flanner, 2020). With coarser grains, the likelihood for light to reflect
off a grain's surface out of the snowpack reduces, lowering the albedo (Wiscombe and Warren, 1980; Gardner and Sharp, 2010;

30 Picard et al., 2012). For example, fresh snow with a small grain radius has a high albedo (typically larger than 0.8), while firn
and ice, for which the grain radius has grown due to metamorphism, have a lower albedo (typically approximately 0.55 for
ice and 0.7 for firn). Likewise, snow grain shape impacts the probability for light to reflect out of the snowpack (Libois et al.,
2013; He et al., 2018a). It is thus essential to consider the spectral albedo of snow and ice when modeling the snowpack or ice
melt.

35 Since incoming solar radiation also varies greatly as a function of wavelength (Gates, 1966; Leckner, 1978), the broadband
albedo, i.e., the wavelength-integrated spectral albedo, is also altered by atmospheric properties, like clouds and water vapour,
and by the solar zenith angle (SZA) (Dang et al., 2015). The SZA impacts the spectral distribution of incoming light, as
Rayleigh scattering is more effective for larger wavelengths, but also alters the angle of incidence into the snowpack (Solomon
et al., 1987; Gardner and Sharp, 2010; Van Dalum et al., 2019). A large SZA results in a shallow angle of incidence, increasing

40 the probability for light to scatter out of the snowpack, which increases the spectral albedo. In addition, upper snow layers are
often characterized by small grains, enhancing the spectral albedo even further. However, this increase of spectral albedo at
large SZA is largely mitigated by the red shift of the incoming radiation due to enhanced Rayleigh scattering in the atmosphere.
During cloudy conditions, radiation is more likely to scatter, changing the weighted average SZA and thus the spectral albedo.
Furthermore, clouds and water vapour alter the spectral distribution of radiation at the surface by filtering out IR radiation.

45 Subsequently, the blue shift of incoming radiation under cloudy conditions leads to an increase of the broadband albedo even
if the snow structure remains unaltered.

RCMs and GCMs commonly perform their radiative calculations for the atmosphere on a limited number of spectral bands.
The albedo of such a spectral band is defined as the narrowband albedo. These models, however, often do not use the nar-
rowband albedo, but determine a broadband albedo instead, bypassing its spectral bands and neglecting any spectral albedo

50 variations. Recently, progress has been made in the development of new snow albedo parameterzations and coupling schemes,
which allows for the use of spectral bands and more physical processes to be included (Libois et al., 2013; Van Dalum et al.,
2019).

In this study, we improve the snow and ice albedo parameterization in the polar version of the Regional Atmospheric Climate
Model (RACMO2) and present version 2.3p3. The polar version of RACMO2 is a model developed to simulate the climate

55 and atmosphere-surface interaction of glaciated regions, in particular Greenland (e.g., Noël et al., 2018) and Antarctica (e.g.,
Van Wessem et al., 2018). The snow albedo scheme of previous RACMO2 versions (2.1 to 2.3p2) uses an adjusted version
of the parameterization of Gardner and Sharp (2010) to derive a broadband albedo. Therefore, RACMO2 until now did not
include explicit spectral albedo or spectral irradiance effects, nor an adequate radiation penetration scheme. Introducing a new
snow albedo parameterization that includes these processes is therefore timely.

RACMO2.3p3 uses a new snow albedo parameterization using the Two-streAm Radiative TransfEr in Snow model (TARTES, Libois et al., 2013) coupled with the Spectral-to-NarrOWBand ALbedo (SNOWBAL) module version 1.2 (Van Dalum et al., 2019). This set-up provides appropriate narrowband albedos for all 14 shortwave spectral bands utilized in RACMO2. TARTES also considers radiation penetration for its surface albedo calculations and provides estimates of energy absorption in the snowpack. Additionally, the new snow albedo parameterization is used to update the ice albedo scheme.

Here, we present and evaluate the broadband and narrowband albedo modeled by RACMO2.3p3 for the GrIS, and compare it with remote sensing data, in-situ observations and the broadband albedo modeled by the previous iteration of RACMO2, version 2.3p2. The remainder of this manuscript is made up of six sections. Section 2 summarizes the changes made in RACMO2 and introduces the remote sensing and in-situ observational data sets. Section 3 and Sect. 4 evaluate the new RACMO2 version with these data sets. Comparisons between the albedo modeled by RACMO2 version 2.3p3 and 2.3p2 are shown in Sect. 5. Finally, the sensitivity to the chosen impurity concentration of snow is analyzed in Sect. 6, and results are discussed and conclusions are drawn in Sect. 7. The impact of the model improvements on the climate, surface mass balance and surface energy balance of the GrIS ice sheet will be discussed in a forthcoming publication.

2 Model and observational data sets

2.1 Regional climate model

The Regional Atmospheric Climate Model (RACMO2), integrates the atmospheric dynamics of the High Resolution Limited Area Model (HIRLAM, Undén et al., 2002), version 5.0.3, with the surface and atmospheric processes of the European Center for Medium-Range Weather Forecasts (ECMWF) Integrated Forecast System (IFS), cycle 33r1 (ECMWF, 2009). The polar version of RACMO2, version 2.3p2, from now on abbreviated to Rp2, is adapted for glaciated regions by using a multilayer snowpack that interacts with the atmosphere and involves processes within the snow column, such as melt and refreezing. Rp2 is introduced in more detail in Noël et al. (2018). At the lateral boundaries, RACMO2 is forced with ERA-Interim data (Dee et al., 2011). In the new RACMO2 version, 2.3p3, from now on abbreviated to Rp3, two components have been adjusted, the multilayer firn module and the snow and ice albedo parameterizations for glaciated regions.

2.1.1 Multilayer firn module updates

In Rp3, the multilayer firn module has been rewritten to improve numerical stability and code readibility. As part of this update, four modifications have been implemented.

Firstly, Rp2 uses a prognostic fresh snow layer, which is effectively a sublayer of the uppermost snow model layer. In Rp3 this fresh snow layer is removed; instead, the uppermost layers are allowed to be very thin, i.e., in the order of millimeters, thus containing fresh snow only. For heat diffusion calculations, these thin layers are treated as a single layer to maintain numerical stability. If melt or refreezing occurs in one of these layers, their individual temperature is estimated obeying the temperature gradient and conserving their combined heat content.

Secondly, in Rp2 layers below a threshold thickness merge with the first layer below. In Rp3, a layer merges with the adjacent layer having most similar density and grain size. Furthermore, undesired numerical diffusion is avoided by implementing mass redistribution if a thin layer merges with a thick layer. A layer containing glacial ice is not allowed to merge with layers that are formed locally, i.e., by snow deposition on this grid point. This allows for the formation and preservation of layers with ice lenses.

Thirdly, internal melt, caused by heating due to radiation penetration, will only thin a subsurface snow layer, i.e., a layer with a density below 700 kg m^{-3}, and not change its density. For ice layers, i.e., with a density larger than 830 kg m^{-3}, only a density reduction takes place and no thinning occurs. For firn with intermediate densities, the induced layer thinning fraction linearly decreases from 1 to 0 between 700 kg m^{-3} and 830 kg m^{-3}. The resulting density is adjusted accordingly. Melting of the uppermost layer always leads to thinning, regardless of its density.

Finally, the initialized ice density is increased from 910 kg m^{-3} to 917 kg m^{-3}. Note that the density of a bare ice layer is usually lower than 917 kg m^{-3}, mimicking air bubbles within the layer.

2.1.2 Snow albedo

Rp2 uses a plane-parallel broadband snow albedo scheme based on Gardner and Sharp (2010), that depends indirectly on wavelength in the form of tuning parameters, and is limited to two snow layers. This albedo scheme parameterizes albedo variations due to a changing SZA, grain radius, cloud cover, impurities, and an altitude-dependent atmospheric optical thickness, the latter for clear-sky conditions (Kuipers Munneke et al., 2011). In RACMO2, the first two snow layers are often very thin, i.e. a few millimeters for fresh snow and up to a few centimeters for older snow, thus effectively neglecting almost all radiation penetration.

In Rp3, the Two-streAm Radiative TransfEr in Snow model (TARTES, Libois et al., 2013) coupled with the Spectral-to-NarrOWBand ALbedo (SNOWBAL) module (Van Dalum et al., 2019) is implemented. TARTES is a spectral albedo model based on the radiative transfer equation (Jiménez-Aquino and Varela, 2005) and asymptotic analytical radiative transfer theory (Kokhanovsky, 2004) assuming Rayleigh scattering, which allows for a vertically inhomogeneous snowpack. Grain radius, grain shape, snow layer density, impurity concentration and type, and SZA are all explicitly resolved. TARTES is able to calculate a spectral albedo for any wavelength between 199 and 3003 nm and returns the absorption of radiation within the snowpack for both incoming direct, i.e., no atmospheric scattering, and diffuse radiation, i.e., light that is scattered by the atmosphere, of which the latter is considered to be a direct beam with a SZA of 53°.

In order to couple TARTES with the IFS physics within RACMO2, which employs 14 contiguous shortwave spectral bands (Fig. 1d), the SNOWBAL module has been developed (Van Dalum et al., 2019). Since both the spectral albedo and the incoming solar radiation can vary within a spectral band, SNOWBAL selects the predefined representative wavelengths for the given atmospheric condition that would provide the correct effective narrowband albedos by TARTES. The representative wavelength depends on the SZA for clear-sky diffuse radiation, SZA and vertically integrated water vapour for clear-sky direct radiation, and ice and liquid water path for cloudy conditions. As full radiation calculations are only performed every hour, the average SZA of the next hour is used as long as the sun is above the horizon. Excluded are bands 13 and 14, for which the narrowband

125 albedo can safely assumed to be zero (Gardner and Sharp, 2010; Van Dalum et al., 2019). For the other bands, three narrowband albedos are determined, i.e., for direct and diffuse radiation for clear-sky conditions, and for diffuse radiation for cloudy conditions. Clear-sky and total-sky narrowband and broadband albedos are then determined using the modeled radiative fluxes. Note that clear-sky and total-sky albedo are identical if no clouds are present. Finally, for evaluation with the seven MODIS narrowband albedos, clear-sky diffuse radiation albedos are also explicitly derived for these bands.

130 In this manuscript, 'albedo' without further specification refers to the broadband albedo. White-sky albedo (WSA) and black-sky albedo (BSA) refer to surfaces illuminated only by diffuse and direct radiation, respectively. If no clouds are present, the WSA and BSA can be combined to a clear-sky albedo.

2.1.3 Bare ice albedo

In Rp2, a background bare ice albedo (BIA) field is defined for the entire ice sheet and used if one of the upper two snow

135 layers are identified as bare ice. The BIA field is prescribed by the lowest five percent of the 16-day diffuse albedo product (MCD43A3v5, Schaaf and Wang (2015)) of 1 km MODIS data, for the period 2000-2015 (Fig. 1a). The MODIS albedo field is resampled to the model grid, and the BIA is limited to values between 0.3 for dark ice in the ablation zone, and 0.55 in the accumulation zone under perennial snow (Noël et al., 2018).

As we do not want to bypass TARTES for bare ice, we derived a representative specific surface area (SSA) and impurity

140 concentration field to be used for bare ice to mimic the broadband MODIS albedos. Firstly, we assume that clean bubble-free ice has an albedo of approximately 0.6 (Reijmer et al., 2001) and that the bare ice albedo is subsequently lowered by standing water, bubbles and impurities, and that MODIS bare ice albedos are valid for clear-sky conditions (Wang et al., 2012; Casey et al., 2017). As TARTES does not use Mie-scattering theory, which would be preferable for ice (Gardner and Sharp, 2010), bubbles cannot be modeled explicitly, nor can water be included. Hence, albedos ranging from 0.30 to 0.55 observed for the

145 GrIS are obtained by increasing the impurity content. Using a semi-infinite layer with the density of ice, a SSA value of 0.788 m^2 kg^{-1} (4.152 mm grain size, which is an order of magnitude larger than the typical grain radius for snow (Warren, 2019)) is found to provide an albedo 0.6 (Fig. 1b). Despite using Rayleigh scattering, the spectral curve in TARTES for this SSA value resembles the expected curve for bare ice quite well, especially in the (infra)red part of the spectrum (Fig. 1d, blue line) (e.g., Dadic et al., 2013), and thus can be used to mimic clean, bubble-free ice.

150 Next, the MODIS bare ice albedo range is converted to an impurity concentration. Using the fitted SSA, ice density and a reference SZA of 60°, which is the largest angle for which the observations of MODIS for the GrIS are still somewhat reliable (Wang and Zender, 2010), together with RACMO2 narrowband irradiance profiles for such conditions, a broadband albedo can be calculated for a range of impurities such that the MODIS albedo range is covered. The resulting impurities vary between 69 ng g^{-1} for an albedo of 0.55, to 2445 ng g^{-1} for an albedo of 0.3 (Fig. 1c), and are saved in a lookup table. This lookup

155 table is used to convert the MODIS albedo field, after resampling to the 11-km grid of RACMO2, to an impurity field feasible for TARTES to use in RACMO2 (Fig. 1b). Adding soot alters, as expected (Doherty et al., 2010; Gardner and Sharp, 2010; He and Flanner, 2020), only the spectral curve in the near-UV and visible part of the spectrum (Fig. 1d). Note that the broadband albedo can still reach values beyond the range indicated in Fig. 1c, depending on atmospheric conditions and SZA.
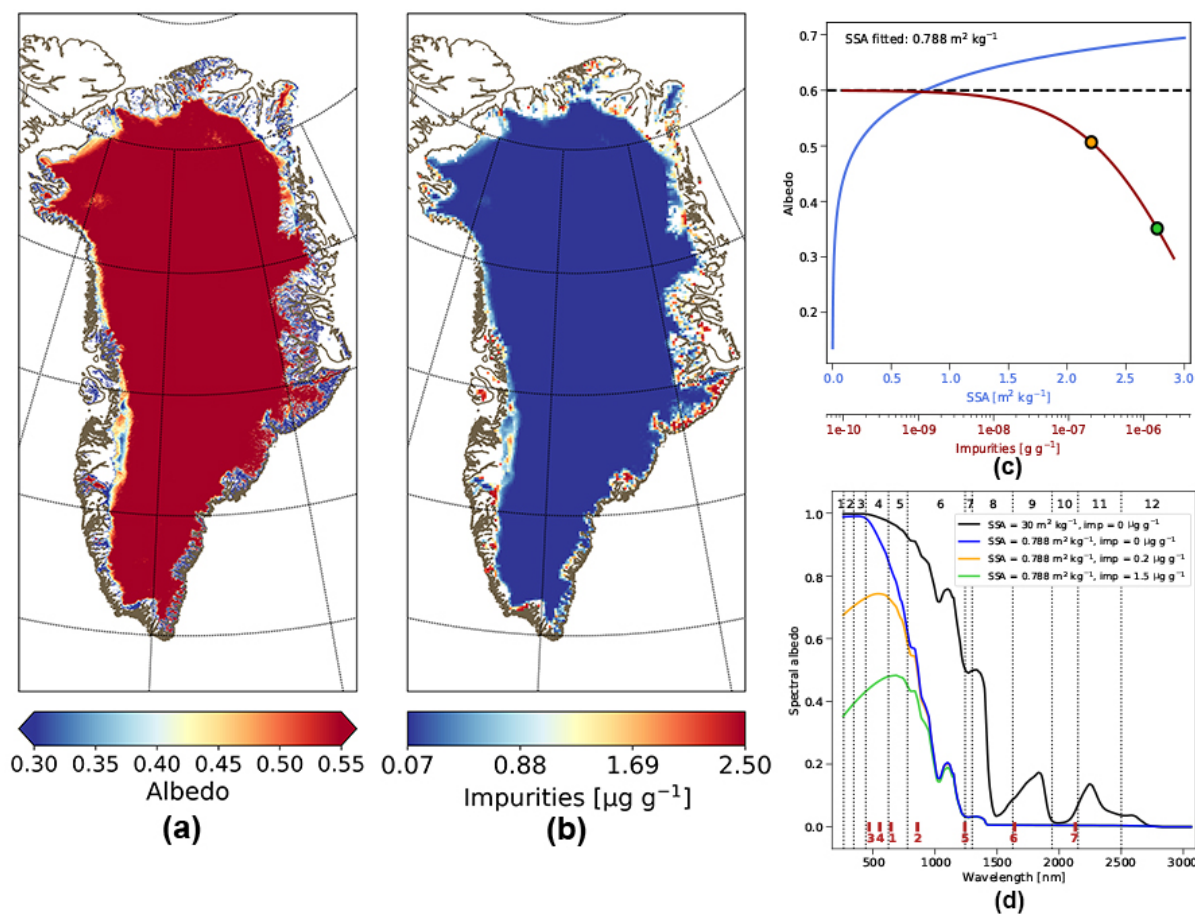
Figure 1. (a) Lowest five percent of the MODIS MCD43A3v5 1 km 16-day clear-sky diffuse albedo field. The albedo is limited between 0.30 and 0.55 for consistency with RACMO2. **(b)** Bare ice impurity field that is implemented in RACMO2.3p3. **(c)** In blue, fitting the SSA to clean bubble-free ice albedo, which is assumed to be 0.6. The fitted SSA equals 0.788 m^2 kg^{-1}. In red, the impurities as a function of albedo required to successfully convert the MODIS albedo field into an impurity field. For both lines, clear-sky conditions are assumed for a SZA of 60° and RACMO2 irradiance profiles are used to convert narrowband to broadband albedo. **(d)** Spectral albedo for clean fresh snow (in black), and for an ice profile with the fitted SSA of 0.788 m^2 kg^{-1} for various impurity concentrations. The first twelve spectral bands of RACMO2 are indicated by vertical dotted lines and black numbers. Red bars and numbers indicate the seven MODIS spectral bands. The albedo for the impurity concentrations of 0.2 and 1.5 µg g^{-1} are indicated with corresponding colored dots in **(c)**.

2.1.4 Superimposed ice

160 Contrary to Rp2, superimposed ice in the new snow scheme is now distinct from glacial ice. However, without additional corrections the typical grain size of these ice layers is 0.7 to 1.0 mm, leading to unrealistically high albedos of approximately 0.7. In order to improve this, a minimum grain radius for superimposed ice is imposed which increases linearly from 0.720

mm for a density of 750 kg m^{-3}, to 4.152 mm for a density of 917 kg m^{-3}. This correction leads to realistic albedos for superimposed ice and exposed ice lenses.

165   2.2   RACMO2 simulations

For all simulations in this manuscript, RACMO2 is run on an 11-km grid of Greenland and its immediate surroundings, for the period 2006 - 2015, using September 2000 to 2005 as spin-up. At the lateral boundaries, RACMO2 is forced with ERA-Interim data (Dee et al., 2011). The only impurity type considered is soot, with a prescribed concentration of 5 ng g^{-1} in snow. Although the concentration of soot in Greenland varies considerably over time and space, RACMO2 only allows for a fixed

170   soot concentration. In the interior, the soot concentration is approximately 3 ng g^{-1} (Chylek et al., 1992; Dang et al., 2015; Doherty et al., 2010). The impact of impurities, however, is known to be underestimated by TARTES, so a higher prescribed concentration is required to model it properly (Tuzet et al., 2017, 2019). The impact of soot is assessed in various sensitivity experiments, which are done between 2011 and 2015, with September 2008 to 2011 as spin-up.

For initialization, the firn-column state, i.e., the layer thickness, snow and ice density, water concentration, temperature and

175   grain size, were taken for all active layers from the Rp2 run on the initialization day, i.e., 1 September 2000. In order to match the specifications of Rp3, glacial ice is identified in each firn column if the continuous set of layers has a density of 899 kg m^{-3} or higher, counted from the bottom of the firn column. Furthermore, the bare ice albedo value is replaced with the bare ice soot concentration and the fresh snow sub-layer data is omitted (see Sect. 2.1.3).

2.3   MODIS snow albedo product

180   The RACMO2 albedo product is evaluated with the Moderate Resolution Imaging Spectroradiometer (MODIS), using the MCD43A3 Version 6 Albedo Model daily dataset using 16-day Terra and Aqua MODIS data for white-sky, i.e., diffuse, and black-sky, i.e., direct, conditions (Wang et al., 2012; Schaaf and Wang, 2015). WSA and BSA are calculated for local solar noon. WSA is preferred for evaluation, as no uncertainties arise concerning SZA, although the difference between the BSA and WSA product is only marginal (Williamson et al., 2016). But note that the MCD43A3 WSA product remains a slightly

185   different albedo product than the clear-sky RACMO2 albedo it evaluates, which includes both direct and diffuse radiation. MCD43A3 provides an albedo product in seven shortwave bands, ranging between 620 and 2155 nm (Fig. 1d, red bars), with a spatial resolution of 500 m (250 m for band 1 and 2). In addition, visible, near-IR and broadband albedo products are provided. In this study, the broadband albedo and seven shortwave band albedos are used for model evaluation.

For comparison with RACMO2, MODIS data are resampled to the 11-km grid of RACMO2. Due to the lack of a proper

190   ice mask for this MODIS field, contamination with non-glaciated grid points cannot be excluded for some grid points at the margin. Therefore, these grid points are omitted if the albedo becomes too low (smaller than 0.25) during summer.

Lhermitte et al. (2014) and Williamson et al. (2016) reported that MODIS captures the albedo evolution well for most of the GrIS, but that it has problems for inhomogeneous regions, like mountain ranges. MODIS albedo also shows a drop in accuracy for SZAs larger than 55°, and becomes physically unrealistic for SZAs larger than 65° (Wang and Zender, 2010;

195   Liu et al., 2009). Therefore, the evaluation with RACMO2 is limited to a SZA of 55° or less. In addition, latitudes north

of 75°N should be excluded, as the noise-to-signal ratio of MODIS becomes too high (Wang and Zender, 2010; Manninen et al., 2019). Consequently, northern Greenland is omitted from the evaluation. As MODIS only measures during clear-sky conditions, some regions have limited coverage. The estimated root-mean-square error (RMSE) and bias of the MCD43 albedo product with respect to in-situ observations according to Stroeve et al. (2013) are 0.067 and 0.022, respectively, indicating that

200   MCD43 overestimates the albedo.
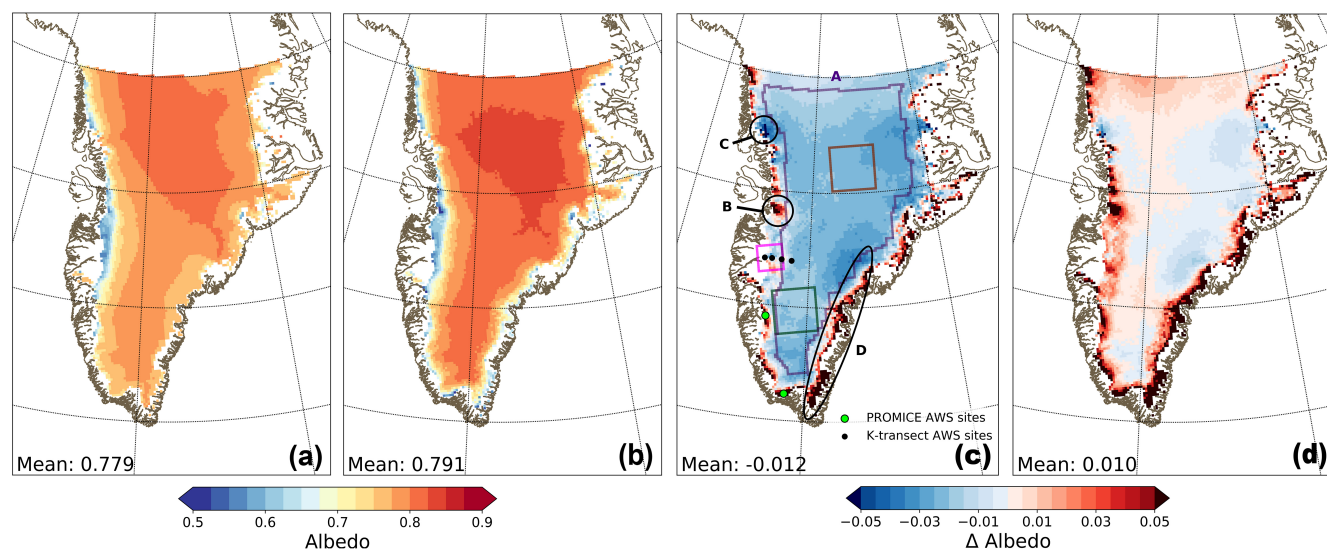
Figure 2. (a) Average 16-days running mean clear-sky RACMO2.3p3 albedo for 15:00 UTC (12:00 LT for most of Greenland) between 2006 and 2015, **(b)** MODIS MCD43A3 white-sky albedo, **(c)** albedo difference between RACMO2.3p3 clear-sky albedo and MODIS MCD43A3 white-sky albedo and **(d)**, like **(c)**, but now after applying a uniform -0.022 bias correction to the MODIS MCD43A3 data. AWS locations of the K-transect are indicated in **(c)** by the black dots, from west to east: S5, S6, S9 and S10. PROMICE AWS NUK-U (north) and QAS-U (south) are indicated by the light-green dots. KAN-M and KAN-U are located close to S10 and between S6 and S9, respectively, but are not shown separately. Extended evaluation is done for the enclosed purple region that is indicated by **A**, for areas **B**, **C** and **D**, and the regions enclosed in the colored boxes.

2.4   In-situ measurements

In-situ observations provide insight in the performance of RACMO2 for total-sky and cloudy conditions, unavailable from remote sensing observations. Therefore, we evaluate the albedo product with the Automatic Weather Station (AWS) data along the Kangerlussuaq-transect (K-transect, Smeets et al., 2018) and with a selection of AWS data of the Programme for Monitoring of the Greenland Ice Sheet (PROMICE) (Van As et al., 2011).

205   The K-transect data used are from AWS sites S5, S6, S9 and S10, and are available for 2006 up to 2015, with an exception for S10, which is only available between 2010 up to 2015. The K-transect is located in southwest Greenland (Fig. 2c) around 67° N. More specifically, S5 and S6 are located in the ablation zone, S9 approximately on the equilibrium line, and S10 in the

accumulation zone. Daily hourly-averaged observations are considered at noon local time in Greenland (15:00 UTC), and a
210 running average of 16 days is taken to fit the temporal sampling of MODIS.

PROMICE AWS are mostly located in the ablation zone. Only AWS sites that cover at least partially the model period and
for which an appropriate grid point can be selected in RACMO2, are selected. Figure 2c shows the location of the PROMICE
stations used in this study. KAN-U and KAN-M are located along the K-transect, NUK-U and QAS-U are located in the
southwest and south, respectively.

215 ## 3 Evaluation using MODIS albedo

In this section, we evaluate and discuss the Rp3 clear-sky albedo output with MODIS WSA for both broadband and narrowband
albedo and discuss processes involved.

3.1 Comparison with MODIS broadband albedo

Figure 2 shows the 2006-2015 average 16-days running mean clear-sky albedo of Rp3 (Fig. 2a) and MODIS WSA (Fig. 2b) at
220 15:00 UTC (local noon for most of Greenland). On average, the spatial patterns are similar, while some local differences can be
observed (Fig. 2c). The domain-averaged bias considering all glaciated grid points is -0.012, indicating a slight underestimation
of the modeled albedo with respect to MODIS WSA. For the interior, indicated by **A** and enclosed within the purple line in
Fig. 2c, which excludes all grid points within five grid points of the margin, we observe an average bias of -0.022, which is
exactly the value reported by Stroeve et al. (2013). Correcting for this MCD43 albedo bias (Fig. 2d), the bias for area **A** reduces
225 to 0.000, supporting excellent agreement in the accumulation zone. Furthermore, only a small overestimation is observed in
the large bare ice region around the K-transect (black dots in Fig. 2c), showing that the new bare ice albedo parameterization
produces adequate results for this region.

Around Jakobshavn (circle indicated by **B** in Fig. 2c), Rp3 considerably overestimates the albedo, especially during the
accumulation season. This region is characterized by rough and heavily crevassed terrain, causing an inhomogeneous snow
230 cover. Rp3, however, evenly distributes snow within a grid cell, that is, patches of snow are not modeled. Consequently,
the albedo of Rp3 is too high, as snow-free areas like hummocks and crevasse openings are not properly captured. Snow
subsequently remains for too long at the surface in Rp3 before melting in the ablation season.

The region indicated by **C**, which typically has only a few decimeters of snow during winter, indicates an underestimation
of Rp3 albedo compared to MODIS. The albedo difference during winter is limited, as this region is less rough than region
235 **B**, but increases during the ablation season. Throughout the summer, Rp3 likely underestimates the snow thickness, leading to
underestimated albedo.

Most pronounced biases can be observed for grid points close to the margin in the southeast (region **D**), but extending
beyond this region. The albedo difference is typically around 0.03, but can be as high as 0.15. The ablation zone in **D** is too
narrow (up to 10 km) to be adequately resolved at the used resolution of 11 km (Noël et al., 2015). Furthermore, the southeast
240 is characterized by heavy snowfall (Ohmura and Reeh, 1991; Mernild et al., 2015), and in combination with the low model
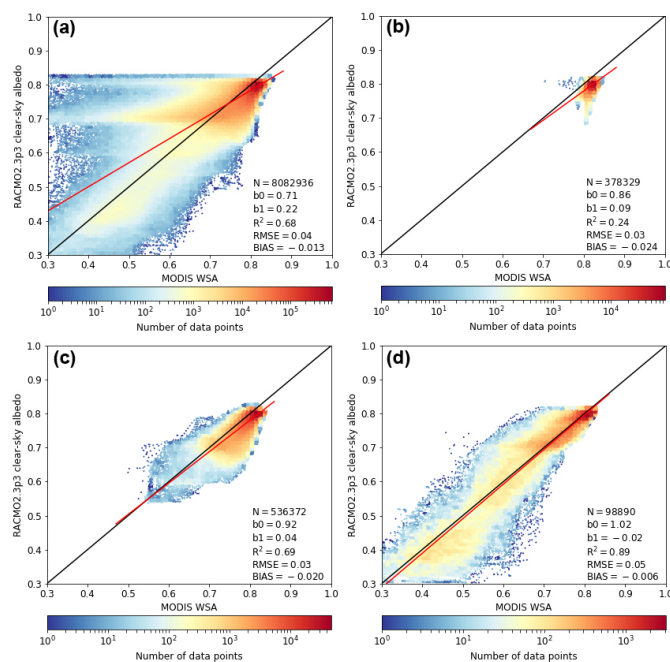
Figure 3. Comparison between 16-days running mean RACMO2.3p3 clear-sky albedo and MODIS MCD43A3 WSA. Every data point represents an observation at a grid point at 15:00 UTC for a day between 2006 and 2015. In black the 1-to-1 line. The red line is the linear regression of the data, with b0 the slope and b1 the intercept. In addition, number of records (N), correlation coefficient (R^2) and root-mean-square error (RMSE) are displayed. Colours indicate number of data points and the bin size is 0.01. **(a)** Displays data for the whole domain, **(b)**, **(c)** and **(d)** the brown, green and pink boxes in Fig. 2c, respectively.

resolution, snow persists at the surface throughout the ablation season in Rp3. Still, the grain radius increases and the albedo drops somewhat during the ablation season, but not as fast as the albedo decline in MODIS. Note that the uncertainty of MODIS is also considerable, as this is mountainous terrain (see Sect. 2.3).

245   Figure 3 correlates the uncorrected MODIS WSA with Rp3 clear-sky albedo at noon on a grid-point level for the whole time span and domain (Fig. 3a) and in various regions (Fig. 3b-d). In general, Rp3 correlates well with MODIS with a low RMSE and bias, but typically underestimates the albedo, as is also observed in Fig. 2. With declining albedos, both Rp3 and MODIS WSA generally follow the same pattern, also in the bare ice regime. There are, however, two distinct outliers visible in Fig. 3a, around Rp3 albedos of 0.81 and 0.70, where Rp3 models fresh and melting snow, respectively, instead of bare ice that MODIS observes. These data points originate from the southeast (area **D** of Fig. 2c, see the previous discussion). The

250 bias for the Summit region (Fig. 3b) is similar to both the bias of area **A** (Fig. 2c) and the bias of the MODIS WSA product (Stroeve et al., 2013). Furthermore, the albedo variability is low for this region, as melt does normally not occur here (except for July 2012 (Nghiem et al., 2012; Bennartz et al., 2013)) and metamorphosis is slow in this cold climate. Figure 3c represents an area in southern Greenland without bare ice, which is characterized by albedo decrease due to rapid snow metamorphism

(Lyapustin et al., 2009). Rp3 performs well for this region. The region shown in Fig. 3d corresponds roughly with the ablation

255 zone of the K-transect. The bias is very low considering the large variability in the ablation zone and the correlation coefficient is high. Both the bare ice and snow albedo schemes perform well and merge smoothly together. Note that the outliers of Fig. 3a are absent around the K-transect, indicating that it is not the bare ice albedo scheme that causes the discrepancies.
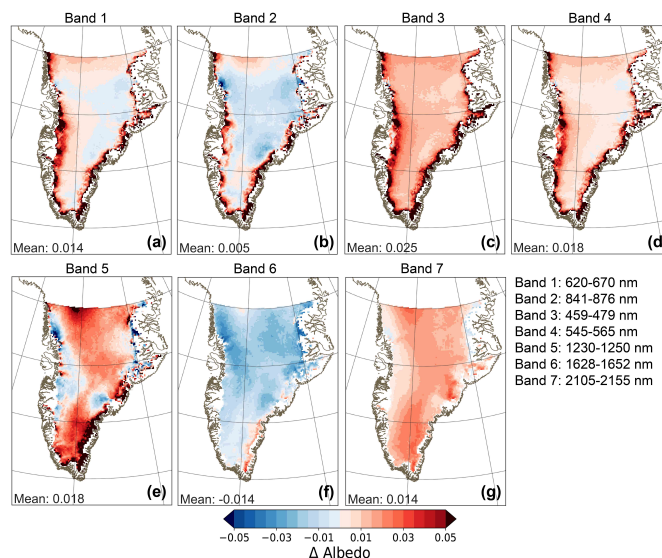
Figure 4. Average albedo difference for 15:00 UTC between RACMO2.3p3 16-days running mean clear-sky diffuse albedo and MODIS MCD43A3 white-sky albedo product, between 2006 and 2015 for **(a)** band 1 to **(g)** 7 (red bands in Fig. 1d). The spectral width of each band is also shown.

3.2 Comparison with MODIS narrowband albedo

MODIS broadband albedo is derived from its seven narrowband sensors (red bands in Fig. 1d). Note that the quality of band 6 is

260 reduced for the AQUA satellite due to instrument failure (Stroeve et al., 2006; Box et al., 2012). To allow for direct comparison with MODIS' narrowband observations, TARTES within Rp3 is also run for wavelengths representative for the seven MODIS bands with diffuse radation. Note that these results are not used to compute a broadband albedo within Rp3. Figure 4 shows the mean spectral albedo difference for these seven bands. Bands that are associated with a strong albedo gradient as a function of wavelength (Fig. 1d) show larger spatial variations (band 2 and 5, Fig. 4b and e) than bands that either have a high (band

265 1, 3 and 4, Fig. 4a, c and d) or low albedo (band 6 and 7, Fig. 4f and g). Overall, differences in the interior are small. Large differences are again observed in area **D**. Bands 1, 3 and 4 show a large positive model bias for the bare ice zone, while the bias for this region is limited for bands 2, 5, 6 and 7. This positive bias for bands 1, 3 and 4 is only present when bare ice is at the surface, illustrating the importance of correctly modeling soot in ice, as soot alters the albedo in particular for these bands (Gardner and Sharp, 2010). Although large quantities of soot have been added for bare ice, as discussed in Sect. 2.1.3,
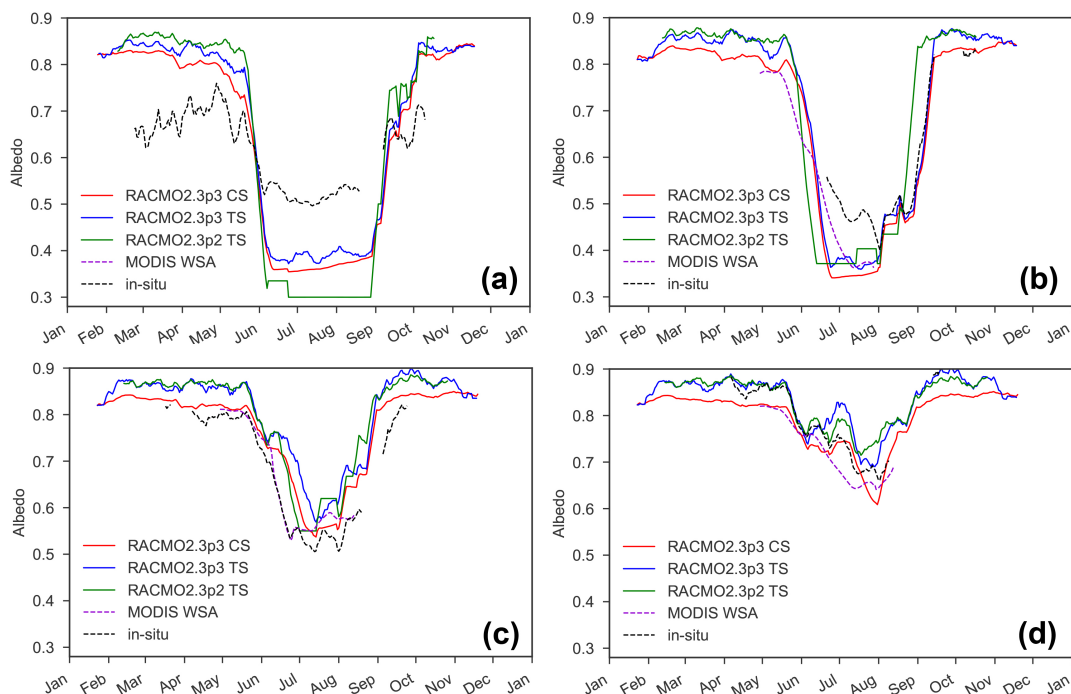
Figure 5. Time series of the average 16-days running mean broadband albedo for 15:00 UTC for RACMO2.3p3 clear-sky (CS) and total-sky (TS) conditions, RACMO2.3p2 TS, MODIS white sky albedo (WSA) and in-situ albedo for 2012 for **(a)** S5, **(b)** S6, **(c)** S9 and **(d)** S10.

270 apparently it is not enough to lower the albedo for bare ice to MODIS values. Elsewhere, Rp3 generally shows small differences with the seven MODIS bands, indicating that the albedo for various wavelengths is captured well.

4   In-situ broadband albedo measurements

Along the K-transect, albedo data are available at S5, S6, S9 and S10 (Fig. 2c) for 15:00 UTC and are shown in Fig. 5 for 2012 and compared with Rp3 clear-sky and total-sky conditions, Rp2 total-sky, and MODIS WSA. S5 is too close to the ice margin
275 for MODIS to produce a reliable albedo at this resolution, and is not included. As the area around this station is characterized by very rough terrain, RACMO2 at this low resolution has trouble reproducing the in-situ albedo.

For S6, Rp3 albedo corresponds well with the measurements, especially when snow returns after the melt season. At the onset of the accumulation season, Rp2 performs considerably worse, as a lack of radiation penetration causes a too rapid albedo increase. As the accumulation season progresses and the snow layers become thicker, the albedo difference between Rp3 and
280 Rp2 diminishes. MODIS WSA fits well with Rp3 clear-sky albedo for bare ice conditions. The resolution of RACMO2 is not sufficient to capture all spatial variations, i.e., the AWS data might not be representative for the full grid point of RACMO2 in which S6 is located.

For S9 (Fig. 5c), both Rp3 and Rp2 total-sky albedo show relatively large deviations with the in-situ measurements during the accumulation season, but the difference of Rp3 clear-sky albedo with MODIS WSA is much smaller. Site S9 is characterized
285 by spatial inhomogeneity, although to a lesser degree than S5 and S6. During the start of the ablation season, superimposed ice persists at the surface, delaying the albedo drop to bare ice values by a few days. Just like at S6, the Rp3 albedo fits better than Rp2 with both in-situ and MODIS observations at the onset of snowfall after summer.

S10 observations (Fig. 5d), which are representative for the lower accumulation zone of Greenland, correspond well with both Rp3 and Rp2. In addition, Rp3 fits with MODIS WSA before the melt season, and performs reasonably well during and
290 after the melt season. 2012 is characterized by a long and intense melt season, explaining the albedo decrease observed in MODIS WSA. The melt season albedo decrease in Rp3, however, is slightly delayed.

5   Comparison with RACMO2.3p2

In this section, we compare the Rp3 albedo product with Rp2 and highlight the differences. Moreover, we investigate the impact that clouds have on the albedo and investigate the seasonal differences.

295 ### 5.1   Broadband albedo differences

Figure 6 shows the 16-days running mean total-sky albedo for 15:00 UTC between 2006 and 2015 for Rp2 and the albedo difference between Rp3 and Rp2. For most of the ice sheet, a small negative difference is observed, i.e., the albedo of Rp3 is slightly lower than Rp2.

In areas **E** in the north-west and **F** in the north-east (Fig. 6b), the albedo of Rp3 is lower than Rp2. Both regions are
300 characterized by limited snowfall, resulting in a shallow snowpack on top of bare ice during the accumulation season for several months (Fig. 7). For September and October, while the sun is still above the horizon, snow layers are thin enough for solar radiation to reach the bare ice layers underneath, lowering the albedo in Rp3. As the accumulation season progresses and the sun rises again above the horizon, the snowpack is already thick enough to prevent solar radiation to reach subsurface bare ice layers in any significant amount, reducing the albedo difference.

305 We also observe a small albedo difference (smaller than 0.01) in the high accumulation region in southeast Greenland (area **D** of figure 2c). For some grid points around the margins, the albedo of Rp3 is considerably higher than Rp2. This difference is more pronounced in areas with exposed bare ice during the ablation season, and is limited to a single grid point bordering non-glaciated tiles. These differences can be traced back to uncertainties in the bare ice albedo field of Rp2, where grid points close to the margin are contaminated with tundra albedo, and an albedo difference with the new model is therefore expected.

310 Figure 8 compares albedo of Rp3 and Rp2 for the entire ice sheet and smaller regions indicated by the colored boxes in Fig. 2c. In general, Rp3 albedo correlates well with the albedo product of Rp2 (Fig. 8a), as the bulk of occurrences are close to the 1-to-1 line (black line). Most of the GrIS is covered in snow, for which the albedo is high (larger than 0.75) and the albedo difference is small (number **1** in Fig. 8a). Snow metamorphism is slightly stronger in Rp3, leading to lower albedos (about 0.75) compared to Rp2 (about 0.8, **2**). Both **1** and **2** typically occur in the interior (Fig. 8b).
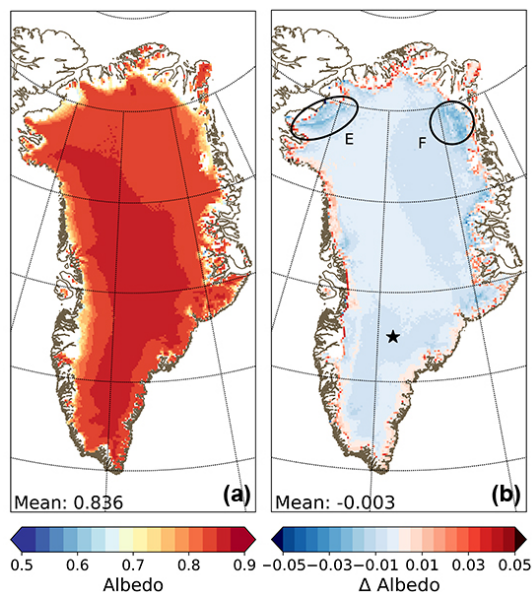
Figure 6. (a) Average 16-days running mean total-sky RACMO2.3p2 albedo and (b) the average albedo difference between RACMO2.3p3 and RACMO2.3p2, for 15:00 UTC between 2006 and 2015, with positive differences indicating that the albedo of RACMO2.3p3 is larger than RACMO2.3p2. Extended evaluation is done for the enclosed region of **E** and **F** and the grid point located at the star.
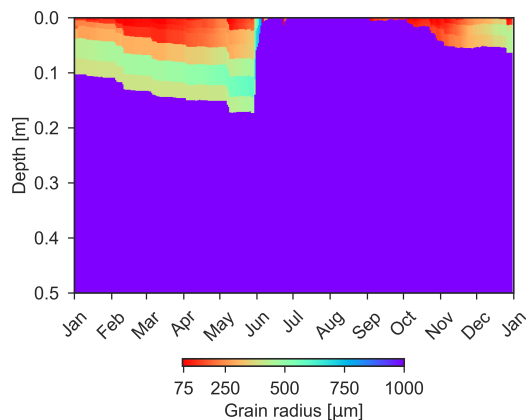
Figure 7. RACMO2.3p3 grain radius of the upper 20 snow layers as a function of depth for 2012, for a grid point within area **E** (Fig. 6b). Bare ice is indicated by a grain radius of 1000 μm.

315   Larger albedo differences occur when firn or ice are close to the surface as radiation penetration lowers Rp3 albedo (**3**). A snow profile similar to Fig. 7 in early June would result in such an albedo difference. For the 0.6 albedo bin of Rp2 (**4**), the albedo of Rp3 is generally 0.05 higher, illustrating that Rp3 seems to have a slower firn-ice transition. In south Greenland (Fig. 8c), processes **1**, **2**, **3** and **4** are all relevant.
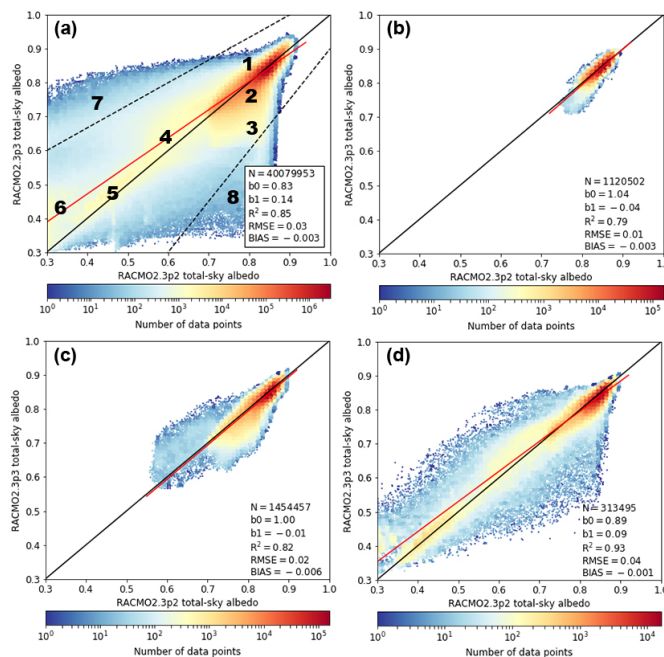
Figure 8. Comparison of 16-days running mean total-sky albedo of RACMO2.3p3 with RACMO2.3p2 for 15:00 UTC, between 2006 and 2015. Similar to Fig. 3, **(a)** shows all ice sheet points, **(b)**, **(c)** and **(d)** only grid cells in the brown, green and pink boxes in Fig. 2c, respectively. Numbers and dashed lines in **(a)** are discussed in the text.

The snow and ice albedo merge well, but the Rp3 albedo is often higher than Rp2 for the ablation zone, i.e., for albedos
320 smaller than 0.6. Still, highest occurrence density is found near the 1-to-1 line (**5**). As the new bare ice albedo parameterization allows variations due to atmospheric conditions, as is described in Sect. 2.1.3, some deviations are expected. That is to say, higher albedos with respect to Rp2 are expected for bare ice, as atmospheric variations usually increase the albedo, e.g., clouds. Additionally, edge errors in Rp2 cause a considerable albedo difference, typically when Rp2 albedo is smaller than 0.35 (**6**). Processes **1** to **6** are all applicable to the region around the K-transect (Fig. 8d), causing a spread for this region that
325 is considerably larger than for the regions in Fig. 8b and Fig. 8c.

The large differences **7** and **8**, that is, all occurrences beyond the dashed lines in Fig. 8a, are not present in the regions considered in Fig. 8b to Fig. 8d. Process **7** occurs almost exclusively next to the ice margin; some in the west, but most in the east and north. In addition to the previously described errors occurring for those points (i.e., mixing with tundra points), snowfall or superimposed ice that is not present in Rp2 can also contribute to the difference. For **8**, most occurrences are
330 associated with area **F** of Fig. 6b and to a lesser extent area **E**, showing the importance of radiation penetration if thin snow layers are located on top of bare ice.

To conclude, the albedo product of Rp3 is often similar to Rp2, but some distinct differences are still notable (Fig. 6 and Fig. 8). All these differences can be well understood in terms of physical processes.

5.2 Clouds

335 In Rp3, SNOWBAL allows spectral variations in the incoming solar radiation to impact the albedo (see Sect. 2.1.2). As clouds absorb mainly in the (infra)red part of the spectrum, a blue shift occurs, which consequently increases the albedo (Dang et al., 2015). The cloud dependence of the albedo parameterization in Rp2 is limited to the cloud optical thickness, neglecting water vapour while no distinction is made between liquid or ice water clouds. Figure 9 shows for a grid point in south-central Greenland (star in Fig. 6b) the total-sky albedo, transmissivity for shortwave radiation in the atmosphere, i.e., the ratio between

340 the top-of-atmosphere (TOA) and surface downwelling radiation, and the fraction of TOA shortwave radiation absorbed in snow as a function of vertically integrated cloud content (VICC), i.e., total liquid water and ice in the atmosphere above a point, for Rp3 and Rp2.

For clear-sky conditions (VICC smaller than 0.05 kg m^{-2}), the albedo in Rp3 is slightly lower than Rp2 (Fig. 9), which is in agreement with previous results. The albedo in Rp3, however, increases more rapidly with VICC than in Rp2, leading

345 to higher albedos for large VICC. Furthermore, the transmissivity decreases slower with VICC than in Rp2 and less radiation is absorbed in snow. For example, for a VICC of 0.3 kg m^{-2}, the broadband albedo, transmissivity and fraction of absorbed energy changes by 0.02, 0.04 and -0.01, respectively. The latter implies that the net SW absorption decreases by approximately 25%. These differences show that as a cloud thickens and the albedo increases in Rp3, more reflected radiation will interact with clouds, eventually raising the transmissivity. Consequently, as these shorter wavelengths now scatter more often and are

350 less likely to be absorbed in the snow, a white-out effect occurs, which is not captured in Rp2.

5.3 Albedo seasonality

Seasonal changes of albedo differences in Rp3 with respect to Rp2 are generally small (Fig. 10). During winter (December, January and February (DJF), Fig. 10a), a homogeneous pattern is present with a small negative difference, that is, the albedo of Rp3 is lower than Rp2. This albedo difference can be mostly attributed to spectral albedo effects, and not as much to radiation

355 penetration, as fresh snow layers are thick enough ice-sheet wide for radiation penetration to be negligible. The winter months are characterized by a high SZA, for which a spectral shift towards larger wavelengths occurs. The spectral albedo of IR radiation is low, hence the broadband albedo drops (Fig. 1d). This effect is weaker in Rp2 than in Rp3 (Van Dalum et al., 2019), leading to a lower albedo. The red shift in irradiance becomes more dominant towards the northern regions as the SZA increases, explaining the northward albedo difference gradient. Albedo differences diminish as spring progresses (March, April

360 and May (MAM), Fig. 10b) and the sun rises higher in the sky.

During summer (June, July and August (JJA), Fig. 10c), larger spatial variations are observed, but the albedo differences in the interior remain small. Along the margins, the albedos can be much higher in Rp3 due to tundra contaminated bare ice albedo in Rp2. Around the equilibrium line in the southwest, a line with higher Rp3 albedos is present, which is due to superimposed ice as is described in Sect. 2.1.4. Small positive albedo differences are observed in wet snow regions, e.g., area **D** in Figure 2c,

365 where snow layers with large grains are located close to the surface. Autumn (September, October and November (SON), Fig.
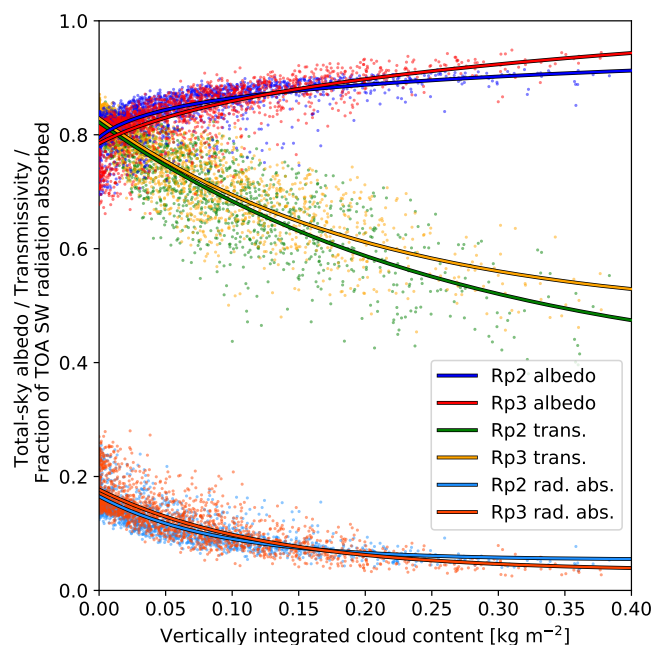
Figure 9. Total-sky albedo, transmissivity (trans.) and fraction of top-of-atmosphere (TOA) shortwave radiation absorbed in the snowpack (rad. abs.) as a function of the vertically integrated cloud content for a grid point in south-central Greenland, indicated with the star in Fig. 6b, for RACMO2.3p3 (Rp3) and RACMO2.3p2 (Rp2). Every point represents a daily-averaged value between 2006 and 2015 if the mean downward TOA shortwave radiation is larger than 200 W m^{-2}. Solid lines show a logarithmic fit for the albedo and an exponential fit for both the transmissivity and the fraction of TOA shortwave radiation absorbed.
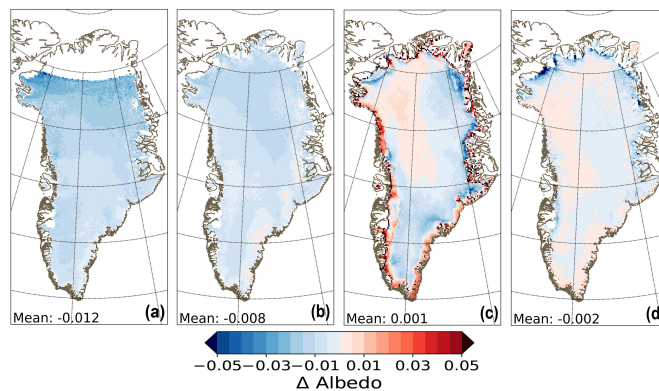
Figure 10. Average 16-days running mean total-sky albedo difference between RACMO2.3p3 and RACMO2.3p2 for **(a)** DJF, **(b)** MAM, **(c)** JJA and **(d)** SON, for 15:00 UTC between 2006 and 2015.

10d) presents very small deviations for most of the ice sheet, as the SZA is too small to make a significant difference, and fresh snow layers accumulate.

6   Sensitivity experiments: soot concentration
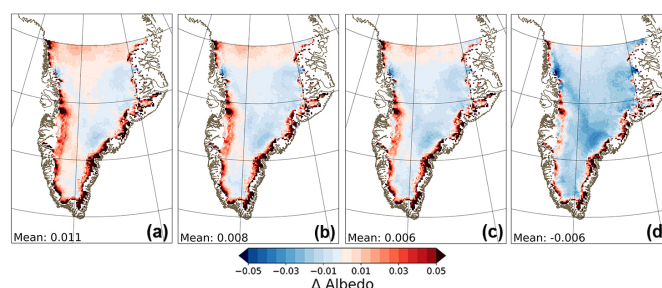
Figure 11. Bias-corrected average 16-days running mean albedo difference for 15:00 UTC between RACMO2.3p3 clear-sky albedo and MODIS MCD43A3 WSA product, between 2011 and 2015, for **(a)** an impurity concentration of 0; **(b)** 5 ng g^{-1}; **(c)** 10 ng g^{-1} and **(d)** 50 ng g^{-1}.

The snow albedo of Rp3 can be tuned with impurity concentration, which in the control run has a fixed value of 5 ng g^{-1}.
370 Snow albedo difference for various impurity concentrations with respect to MODIS WSA is shown in Fig. 11 (2011 - 2015). Excluding all grid points within five grid points of the margin, the mean bias becomes 0.001, -0.002, -0.004 and -0.015 for impurity concentrations of 0, 5, 10 and 50 ng g^{-1}, respectively. The sensitivity to impurity concentration is generally low except for very high concentrations, e.g., 50 ng g^{-1}.

Results for a selection of K-transect and PROMICE observational sites (Fig. 2c) that are sufficiently far away from the
375 ice margin are shown in Fig. 12. Figure 12a is a normalized Taylor diagram (Taylor, 2001) and Fig. 12b shows the bias, misrepresented variability, which is defined as $\sqrt{\mathrm{RMSE}^2 - \mathrm{bias}^2}$, and RMSE, all scaled with the standard deviation in the observations.

In a Taylor diagram, the azimuthal position illustrates the correlation coefficient, the radial distance to the origin the standard deviation and quarter circles with its origin at the 1.0 standard deviation the misrepresented variability. A data set matches the
380 observations perfectly if it is located at the star in Fig. 12a, i.e., with a correlation coefficient and standard deviation of 1 and a misrepresented variability of 0. Data sets located away from the star but on the dashed line have the same variance as the observations, but do not correlate perfectly, leading to a higher misrepresented variability. Data sets close to the origin and close to the y axis, for example, are characterized by an underestimation of the standard deviation and a low correlation coefficient, while data sets beyond the dashed line and close to the x axis overestimate the standard deviation, but have a high correlation
385 coefficient. Similarly, the misrepresented variability is illustrated on the y axis, bias on the x axis and the RMSE on semi circles in Fig. 12b, with data sets performing better close to the origin.

Model performance varies for each observational site, but the sensitivity to small impurity concentrations is generally low. High concentrations of impurities such as 50 ng g^{-1}, on the other hand, alter the albedo considerably, reducing the quality of Rp3 for almost all stations. For NUK-U and QAS-U, which are both located in south Greenland and within 50 km of the ice margin, RACMO2 correlates relatively well, but severely underestimates variability and shows a large bias. As the ice margins are characterized by a high soot concentration (Doherty et al., 2010), a higher modeled soot concentrations consequently performs somewhat better for these locations. Snow cover in RACMO2 is also too homogeneous and similar processes that we discussed for area **B** and **D** of Fig. 2c occur. Additionally, RACMO2 is known to overestimate snowfall for QAS-U, inhibiting bare ice to surface (Noël et al., 2018). For S10 and KAN-M, which are most representative for the interior of the ice sheet, the differences between Rp3 with impurity concentration of 5 and 10 ng g^{-1} and to a lesser degree also with 0 ng g^{-1} and Rp2, are small and in good agreement with observations. To summarize, as the sensitivity of Rp3 to small impurity quantities is low and the snow albedo is generally in good agreement with observations, an ice-sheet wide impurity concentration of 5 ng g^{-1} is a safe choice and for the interior is in good agreement with observations (Fig. 11b).

7   Summary and conclusions

We evaluated the new spectrally-dependent snow and ice albedo parameterization in RACMO2, based on TARTES and coupled by SNOWBAL, for the Greenland ice sheet. The albedo correlates well with the MODIS MCD43A3 white-sky albedo product for both broadband and its seven spectral bands, and performs especially well in the interior. Some discrepancies around the margins are observed, which can be partly ascribed to resolution problems and excessive modeled snowfall, but also to uncertainty in the MODIS product. Around the K-transect, for which many observations are available, the snow and ice albedo in RACMO2 show acceptable small deviations with in-situ and MODIS observations.

With respect to the previous albedo parameterization of RACMO2, slightly lower broadband albedos are modeled. Although large broadband albedo differences at the margins are due to an error in the old version, most changes can be ascribed to improved physics. Radiation penetration, subsurface heating, the inclusion of narrowband albedo and spectral shifts due to solar zenith angle, water vapour and both ice and water clouds are now all incorporated.

There is, however, still room for improvement. The soot concentration for snow is fixed in RAMCO2, while it can change considerably over space and time (Chylek et al., 1992; Doherty et al., 2010; Van Angelen et al., 2012; Dang et al., 2015). Although RACMO2 shows a low sensitivity to small impurity concentrations, a prognostic soot model for snow prescribing a dynamic one-dimensional soot concentration profile is still preferable. Furthermore, no other impurity types are included.

We have also improved the bare ice albedo field by coupling it with TARTES and defining a fictitious grain size, which allows the broadband bare ice albedo to vary with atmospheric conditions. Nevertheless, a proper bare ice albedo module would still be preferable, as for example, a process like darkening due to biological activity is not incorporated, which may become important for future projections (Tedesco et al., 2016; Tedstone et al., 2019). TARTES is based on Rayleigh scattering, while an ice albedo module with Mie-scattering is required (Gardner and Sharp, 2010).
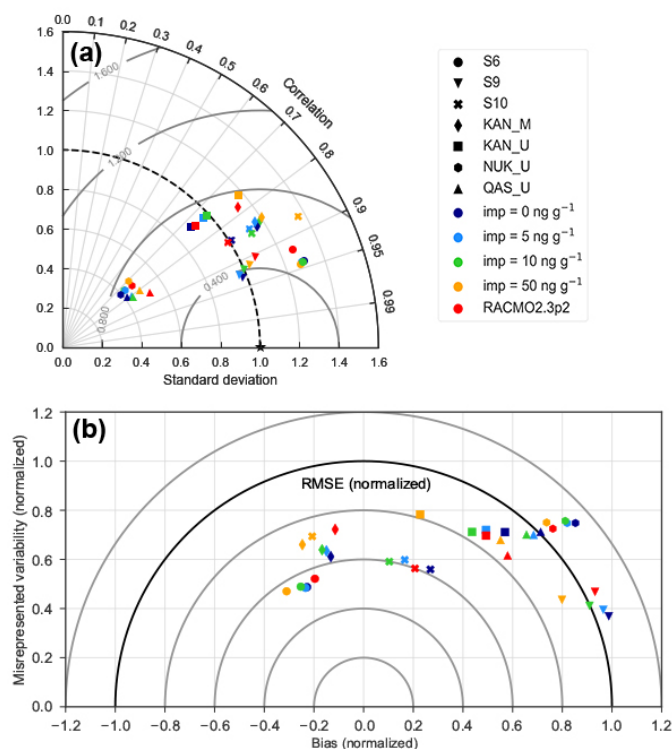
Figure 12. (**a**) Normalized Taylor diagram (Taylor, 2001) for 16-days running mean total-sky albedo of RACMO2.3p3 with various impurity concentrations and RACMO2.3p2 with respect to a selection of K-transect and PROMICE in-situ observations for 15:00 UTC between 2011 and 2015. The standard deviation is illustrated by the radial distance to the origin, the correlation coefficient by the azimuthal position and the misrepresented variability, defined as $\sqrt{\mathrm{RMSE}^2 - \mathrm{bias}^2}$, by quarter circles with its origin at the 1.0 standard deviation. (**b**) Extension to the Taylor diagram, which shows the misrepresented variability on the y axis, bias on the x axis and RMSE on semi circles from the origin. All data is normalized with respect to in-situ observations.

Evaluation of the narrowband albedo of RACMO2 remains limited, as most of the spectral bands of MODIS are located
420 at the edge of rather large bands of RACMO2 and hence cannot be compared directly. To solve this, we have run TARTES specifically for diffuse radiation for the seven bands of MODIS. For these bands, differences between modeled albedo and observations are low. In the bare ice zone, band 1, 3 and 4, which are within the visible light part of the spectrum, show a larger narrowband albedo bias than the other bands. Larger spatial variations are observed for bands 2 and 5, which are characterized by a strong sub-band spectral albedo gradient.

425 To conclude, the new snow and ice albedo scheme of RACMO2 performs very well compared to remote sensing and in-situ observations for the Greenland ice sheet. Differences with the previous version are generally small, but where differences are observed, the new processes lead to improved broadband albedo estimates. The improvement of the albedo scheme of RACMO2 will enhance its ability to make future climate projections. In a forthcoming publication, we assess the impact of the

new snow and ice albedo scheme on the surface mass balance, surface energy balance and subsurface energy absorption of the
430 Greenland ice sheet.

Author contributions. CTvD, WJvdB and MRvdB started and decided the scope of this study and analyzed the results. CTvD implemented the new snow albedo scheme in the model, performed the simulations and led the writing of the manuscript. SL processed and provided remote sensing data. All authors contributed to discussions on the manuscript.

Data availability. RACMO2.3p3 monthly-averaged data for downward and net shortwave radiation for total-sky and clear-sky conditions
435 at 11 km for Greenland (September 2000-2018) can be found here: https://doi.org/10.5281/zenodo.3763442. More RACMO2.3p3 data are available from the authors.

Competing interests. The authors declare that they have no conflict of interest.

Acknowledgements. We acknowledge financial support from the Netherlands Organization for Scientific Research (NWO) and the ECMWF for computational time on their supercomputers.

References

Bennartz, R., Shupe, M. D., Turner, D. D., Walden, V. P., Steffen, K., Cox, C. J., Kulie, M. S., Miller, N. B., and Pettersen, C.: July 2012 Greenland melt extent enhanced by low-level liquid clouds, Nature, 496, 83–86, https://doi.org/10.1038/nature12002, 2013.

Box, J. E., Fettweis, X., Stroeve, J. C., Tedesco, M., Hall, D. K., and Steffen, K.: Greenland ice sheet albedo feedback: thermodynamics and atmospheric drivers, The Cryosphere, 6, 821–839, https://doi.org/10.5194/tc-6-821-2012, 2012.

Casey, K. A., Polashenski, C. M., Chen, J., and Tedesco, M.: Impact of MODIS sensor calibration updates on Greenland Ice Sheet surface reflectance and albedo trends, The Cryosphere, 11, 1781–1795, https://doi.org/10.5194/tc-11-1781-2017, 2017.

Chylek, P., Johnson, B., and Wu, H.: Black carbon concentration in a Greenland Dye-3 Ice Core, Geophysical Research Letters, 19, 1951–1953, https://doi.org/10.1029/92GL01904, 1992.

Dadic, R., Mullen, P. C., Schneebeli, M., Brandt, R. E., and Warren, S. G.: Effects of bubbles, cracks, and volcanic tephra on the spectral albedo of bare ice near the Transantarctic Mountains: Implications for sea glaciers on Snowball Earth, Journal of Geophysical Research: Earth Surface, 118, 1658–1676, 2013.

Dang, C., Brandt, R. E., and Warren, S. G.: Parameterizations for narrowband and broadband albedo of pure snow and snow containing mineral dust and black carbon, Journal of Geophysical Research: Atmospheres, 120, 5446–5468, https://doi.org/10.1002/2014JD022646, 2015.

Dee, D. P., Uppala, S. M., Simmons, A. J., Berrisford, P., Poli, P., Kobayashi, S., Andrae, U., Balmaseda, M. A., Balsamo, G., Bauer, P., Bechtold, P., Beljaars, A. C. M., van de Berg, L., Bidlot, J., Bormann, N., Delsol, C., Dragani, R., Fuentes, M., Geer, A. J., Haimberger, L., Healy, S. B., Hersbach, H., Hólm, E. V., Isaksen, L., Kållberg, P., Köhler, M., Matricardi, M., McNally, A. P., Monge-Sanz, B. M., Morcrette, J.-J., Park, B.-K., Peubey, C., de Rosnay, P., Tavolato, C., Thépaut, J.-N., and Vitart, F.: The ERA-Interim reanalysis: configuration and performance of the data assimilation system, Quarterly Journal of the Royal Meteorological Society, 137, 553–597, https://doi.org/10.1002/qj.828, 2011.

Doherty, S. J., Warren, S. G., Grenfell, T. C., Clarke, A. D., and Brandt, R. E.: Light-absorbing impurities in Arctic snow, Atmospheric Chemistry and Physics, 10, 11647–11680, https://doi.org/10.5194/acp-10-11647-2010, 2010.

Dumont, M., Brun, E., Picard, G., Michou, M., Libois, Q., Petit, J.-R., Geyer, M., Morin, S., and Josse, B.: Contribution of light-absorbing impurities in snow to Greenland's darkening since 2009, Nature Geoscience, 7, 509–512, https://doi.org/10.1038/ngeo2180, 2014.

ECMWF: Part IV: Physical Processes, IFS Documentation, ECMWF, operational implementation 3 June 2008, 2009.

Gardner, A. S. and Sharp, M. J.: A review of snow and ice albedo and the development of a new physically based broadband albedo parameterization, Journal of Geophysical Research: Earth Surface, 115, https://doi.org/10.1029/2009JF001444, f01009, 2010.

Gates, D. M.: Spectral Distribution of Solar Radiation at the Earth's Surface, Science, 151, 523–529, http://www.jstor.org/stable/1717033, 1966.

Hansen, J. and Nazarenko, L.: Soot climate forcing via snow and ice albedos, Proceedings of the National Academy of Sciences, 101, 423–428, https://doi.org/10.1073/pnas.2237157100, 2004.

He, C. and Flanner, M.: Snow Albedo and Radiative Transfer: Theory, Modeling, and Parameterization, pp. 67–133, Springer International Publishing, Cham, https://doi.org/10.1007/978-3-030-38696-2_3, 2020.

He, C., Liou, K.-N., Takano, Y., Yang, P., Qi, L., and Chen, F.: Impact of Grain Shape and Multiple Black Carbon Internal Mixing on Snow Albedo: Parameterization and Radiative Effect Analysis, Journal of Geophysical Research: Atmospheres, 123, 1253–1268, https://doi.org/10.1002/2017JD027752, 2018a.

He, T., Liang, S., Wang, D., Cao, Y., Gao, F., Yu, Y., and Feng, M.: Evaluating land surface albedo estimation from Landsat MSS, TM, ETM+, and OLI data based on the unified direct estimation approach, Remote Sensing of Environment, 204, 181 – 196, https://doi.org/10.1016/j.rse.2017.10.031, 2018b.

480 Jakobs, C. L., Reijmer, C. H., Kuipers Munneke, P., König-Langlo, G., and van den Broeke, M. R.: Quantifying the snowmelt–albedo feedback at Neumayer Station, East Antarctica, The Cryosphere, 13, 1473–1485, https://doi.org/10.5194/tc-13-1473-2019, 2019.

Jiménez-Aquino, J. I. and Varela, J. R.: Two stream approximation to radiative transfer equation: An alternative method of solution, Revista Mexicana de Fisica, 51, 82–86, http://adsabs.harvard.edu/abs/2005RMxF...51...82J, 2005.

King, M. D., Platnick, S., Yang, P., Arnold, G. T., Gray, M. A., Riedi, J. C., Ackerman, S. A., and Liou, K.-N.: Remote Sensing of Liquid
485 Water and Ice Cloud Optical Thickness and Effective Radius in the Arctic: Application of Airborne Multispectral MAS Data, Journal of Atmospheric and Oceanic Technology, 21, 857–875, https://doi.org/10.1175/1520-0426(2004)021<0857:RSOLWA>2.0.CO;2, 2004.

Kokhanovsky, A. A.: Light scattering Media Optics: Problems and Solutions, Springer, 2004.

Kuipers Munneke, P., van den Broeke, M. R., Lenaerts, J. T. M., Flanner, M. G., Gardner, A. S., and van de Berg, W. J.: A new albedo parameterization for use in climate models over the Antarctic ice sheet, Journal of Geophysical Research: Atmospheres, 116,
490 https://doi.org/10.1029/2010JD015113, 2011.

Leckner, B.: The spectral distribution of solar radiation at the Earth's surface elements of a model, Solar Energy, 20, 143 – 150, https://doi.org/10.1016/0038-092X(78)90187-1, 1978.

Lhermitte, S., Abermann, J., and Kinnard, C.: Albedo over rough snow and ice surfaces, The Cryosphere, 8, 1069–1086, https://doi.org/10.5194/tc-8-1069-2014, 2014.

495 Libois, Q., Picard, G., France, J. L., Arnaud, L., Dumont, M., Carmagnola, C. M., and King, M. D.: Influence of grain shape on light penetration in snow, Cryosphere, 7, 1803–1818, https://doi.org/10.5194/tc-7-1803-2013, 2013.

Liu, J., Schaaf, C., Strahler, A., Jiao, Z., Shuai, Y., Zhang, Q., Roman, M., Augustine, J. A., and Dutton, E. G.: Validation of Moderate Resolution Imaging Spectroradiometer (MODIS) albedo retrieval algorithm: Dependence of albedo on solar zenith angle, Journal of Geophysical Research: Atmospheres, 114, D01 106, https://doi.org/10.1029/2008JD009969, 2009.

500 Lyapustin, A., Tedesco, M., Wang, Y., Aoki, T., Hori, M., and Kokhanovsky, A.: Retrieval of snow grain size over Greenland from MODIS, Remote Sensing of Environment, 113, 1976 – 1987, https://doi.org/10.1016/j.rse.2009.05.008, 2009.

Manninen, T., Jääskeläinen, E., and Riihelä, A.: Black and White-Sky Albedo Values of Snow: In Situ Relationships for AVHRR-Based Estimation Using CLARA-A2 SAL, Canadian Journal of Remote Sensing, 45, 350–367, https://doi.org/10.1080/07038992.2019.1632177, 2019.

505 Mernild, S. H., Hanna, E., McConnell, J. R., Sigl, M., Beckerman, A. P., Yde, J. C., Cappelen, J., Malmros, J. K., and Steffen, K.: Greenland precipitation trends in a long-term instrumental climate context (1890-2012): evaluation of coastal and ice core records, International Journal of Climatology, 35, 303–320, https://doi.org/10.1002/joc.3986, 2015.

Nghiem, S. V., Hall, D. K., Mote, T. L., Tedesco, M., Albert, M. R., Keegan, K., Shuman, C. A., DiGirolamo, N. E., and Neumann, G.: The extreme melt across the Greenland ice sheet in 2012, Geophysical Research Letters, 39, L20 502, https://doi.org/10.1029/2012GL053611,
510 2012.

Noël, B., van de Berg, W. J., van Meijgaard, E., Kuipers Munneke, P., van de Wal, R. S. W., and van den Broeke, M. R.: Evaluation of the updated regional climate model RACMO2.3: summer snowfall impact on the Greenland Ice Sheet, The Cryosphere, 9, 1831–1844, https://doi.org/10.5194/tc-9-1831-2015, 2015.

Noël, B., van de Berg, W. J., van Wessem, J. M., van Meijgaard, E., van As, D., Lenaerts, J. T. M., Lhermitte, S., Kuipers Munneke, P.,
515   Smeets, C. J. P. P., van Ulft, L. H., van de Wal, R. S. W., and van den Broeke, M. R.: Modelling the climate and surface mass balance of
polar ice sheets using RACMO2 – Part 1: Greenland (1958–2016), The Cryosphere, 12, 811–831, https://doi.org/10.5194/tc-12-811-2018,
2018.

Ohmura, A. and Reeh, N.: New precipitation and accumulation maps for Greenland, Journal of Glaciology, 37, 140–148,
https://doi.org/10.3189/S0022143000042891, 1991.

520   Picard, G., Domine, F., Krinner, G., Arnaud, L., and Lefebvre, E.: Inhibition of the positive snow-albedo feedback by precipitation in interior
Antarctica, Nature Climate Change, 2, 795–798, https://doi.org/10.1038/nclimate1590, 2012.

Picard, G., Libois, Q., Arnaud, L., Verin, G., and Dumont, M.: Development and calibration of an automatic spectral albedometer to estimate
near-surface snow SSA time series, The Cryosphere, 10, 1297–1316, https://doi.org/10.5194/tc-10-1297-2016, 2016.

Reijmer, C. H., Bintanja, R., and Greuell, W.: Surface albedo measurements over snow and blue ice in thematic mapper bands 2 and 4 in Dron-
525   ning Maud Land, Antarctica, Journal of Geophysical Research: Atmospheres, 106, 9661–9672, https://doi.org/10.1029/2000JD900718,
2001.

Schaaf, C. and Wang, Z.: MCD43A3 MODIS/Terra+Aqua BRDF/Albedo Daily L3 Global - 500m V006, NASA EOSDIS Land Processes
DAAC, https://doi.org/10.5067/MODIS/MCD43A3.006, 2015.

Smeets, P. C. J. P., Munneke, P. K., van As, D., van den Broeke, M. R., Boot, W., Oerlemans, H., Snellen, H., Reijmer, C. H., and van de
530   Wal, R. S. W.: The K-transect in west Greenland: Automatic weather station data (1993-2016), Arctic, Antarctic, and Alpine Research,
50, S100 002, https://doi.org/10.1080/15230430.2017.1420954, 2018.

Solomon, S., Schmeltekopf, A. L., and Sanders, R. W.: On the interpretation of zenith sky absorption measurements, Journal of Geophysical
Research: Atmospheres, 92, 8311–8319, https://doi.org/10.1029/JD092iD07p08311, 1987.

Stroeve, J., Box, J. E., Wang, Z., Schaaf, C., and Barrett, A.: Re-evaluation of MODIS MCD43 Greenland albedo accuracy and trends,
535   Remote Sensing of Environment, 138, 199 – 214, https://doi.org/10.1016/j.rse.2013.07.023, 2013.

Stroeve, J. C., Box, J. E., and Haran, T.: Evaluation of the MODIS (MOD10A1) daily snow albedo product over the Greenland ice sheet,
Remote Sensing of Environment, 105, 155 – 171, https://doi.org/10.1016/j.rse.2006.06.009, 2006.

Taylor, K. E.: Summarizing multiple aspects of model performance in a single diagram, Journal of Geophysical Research: Atmospheres, 106,
7183–7192, https://doi.org/10.1029/2000JD900719, 2001.

540   Tedesco, M., Doherty, S., Fettweis, X., Alexander, P., Jeyaratnam, J., and Stroeve, J.: The darkening of the Greenland ice sheet: Trends,
drivers and projections (1981-2100), The Cryosphere, 10, 477–496, https://doi.org/10.5194/tc-10-477-2016, 2016.

Tedstone, A. J., Cook, J. M., Williamson, C. J., Hofer, S., McCutcheon, J., Irvine-Fynn, T., Gribbin, T., and Tranter, M.: Algal
growth and weathering crust structure drive variability in Greenland Ice Sheet ice albedo, The Cryosphere Discussions, 2019, 1–24,
https://doi.org/10.5194/tc-2019-131, 2019.

545   Tuzet, F., Dumont, M., Lafaysse, M., Picard, G., Arnaud, L., Voisin, D., Lejeune, Y., Charrois, L., Nabat, P., and Morin, S.: A multilayer
physically based snowpack model simulating direct and indirect radiative impacts of light-absorbing impurities in snow, The Cryosphere,
11, 2633–2653, https://doi.org/10.5194/tc-11-2633-2017, 2017.

Tuzet, F., Dumont, M., Arnaud, L., Voisin, D., Lamare, M., Larue, F., Revuelto, J., and Picard, G.: Influence of light-absorbing particles on
snow spectral irradiance profiles, The Cryosphere, 13, 2169–2187, https://doi.org/10.5194/tc-13-2169-2019, 2019.

550   Undén, P., Rontu, L., Jarvinen, H., Lynch, P., Calvo Sánchez, F., Cats, G., Cuxart, J., Eerola, K., Fortelius, C., García-Moya, J., and Jones,
C.: HIRLAM-5 Scientific Documentation, 2002.

Van Angelen, J. H., Lenaerts, J. T. M., Lhermitte, S., Fettweis, X., Kuipers Munneke, P., Van den Broeke, M. R., Van Meijgaard, E., and Smeets, C. J. P. P.: Sensitivity of Greenland Ice Sheet surface mass balance to surface albedo parameterization: a study with a regional climate model, The Cryosphere, 6, 1175–1186, https://doi.org/10.5194/tc-6-1175-2012, 2012.

555 Van As, D., Fausto, R., Ahlstrøm, A., Andersen, S., Andersen, M., Citterio, M., Edelvang, K., Gravesen, P., Machguth, H., Nick, F., Nielsen, S., and Weidick, A.: Programme for Monitoring of the Greenland Ice Sheet (PROMICE): first temperature and ablation record, Geological Survey of Denmark and Greenland Bulletin, pp. 73–76, 2011.

Van As, D., Fausto, R. S., Colgan, W. T., Box, J. E., Ahlstrøm, A. P., Andersen, S. B., Andersen, M. L., Charalampidis, C., Citterio, M., Edelvang, K., Jensen, T. S., Larsen, S. H., Machguth, H., Nielsen, S., Veicherts, M., and Weidick, A.: Darkening of the Greenland ice

560 sheet due to the melt-albedo feedback observed at PROMICE weather stations, Geological Survey of Denmark and Greenland Bulletin, 28, 69–72, 2013.

Van Dalum, C. T., Van de Berg, W. J., Libois, Q., Picard, G., and Van den Broeke, M. R.: A module to convert spectral to narrowband snow albedo for use in climate models: SNOWBAL v1.2, Geoscientific Model Development, 12, 5157–5175, https://doi.org/10.5194/gmd-12-5157-2019, 2019.

565 Van den Broeke, M. R., Reijmer, C. H., Van As, D., and Oerlemans, J.: Seasonal cycles of Antarctic surface energy balance form automatic weather stations, Annals of Glaciology, 43, 131–139, https://doi.org/10.3189/172756405781813168, 2005.

Van Wessem, J. M., Van de Berg, W. J., Noël, B. P. Y., Van Meijgaard, E., Amory, C., Birnbaum, G., Jakobs, C. L., Krüger, K., Lenaerts, J. T. M., Lhermitte, S., Ligtenberg, S. R. M., Medley, B., Reijmer, C. H., Van Tricht, K., Trusel, L. D., Van Ulft, L. H., Wouters, B., Wuite, J., and Van den Broeke, M. R.: Modelling the climate and surface mass balance of polar ice sheets using RACMO2 – Part 2: Antarctica

570 (1979–2016), The Cryosphere, 12, 1479–1498, https://doi.org/10.5194/tc-12-1479-2018, 2018.

Wang, X. and Zender, C. S.: MODIS snow albedo bias at high solar zenith angles relative to theory and to in situ observations in Greenland, Remote Sensing of Environment, 114, 563 – 575, https://doi.org/10.1016/j.rse.2009.10.014, 2010.

Wang, Z., Schaaf, C. B., Chopping, M. J., Strahler, A. H., Wang, J., Román, M. O., Rocha, A. V., Woodcock, C. E., and Shuai, Y.: Evaluation of Moderate-resolution Imaging Spectroradiometer (MODIS) snow albedo product (MCD43A) over tundra, Remote Sensing of

575 Environment, 117, 264 – 280, https://doi.org/10.1016/j.rse.2011.10.002, 2012.

Warren, S. G.: Optical properties of ice and snow, Philosophical Transactions of the Royal Society A, 377, 20180161, https://doi.org/10.1098/rsta.2018.0161, 2019.

Warren, S. G. and Wiscombe, W. J.: A Model for the Spectral Albedo of Snow. II: Snow Containing Atmospheric Aerosols, Journal of the Atmospheric Sciences, 37, 2734–2745, https://doi.org/10.1175/1520-0469(1980)037<2734:AMFTSA>2.0.CO;2, 1980.

580 Warren, S. G., Brandt, R. E., and Grenfell, T. C.: Visible and near-ultraviolet absorption spectrum of ice from transmission of solar radiation into snow, Appl. Opt., 45, 5320–5334, https://doi.org/10.1364/AO.45.005320, 2006.

Williamson, S. N., Copland, L., and Hik, D. S.: The accuracy of satellite-derived albedo for northern alpine and glaciated land covers, Polar Science, 10, 262 – 269, https://doi.org/10.1016/j.polar.2016.06.006, iSAR-4/ICARPIII, Science Symposium of ASSW2015, 2016.

Wiscombe, W. J. and Warren, S. G.: A Model for the Spectral Albedo of Snow. I: Pure Snow, Journal of the Atmospheric Sciences, 37,

585 2712–2733, https://doi.org/10.1175/1520-0469(1980)037<2712:AMFTSA>2.0.CO;2, 1980.

Wyser, K. and Yang, P.: Average ice crystal size and bulk short-wave single-scattering properties of cirrus clouds, Atmospheric Research, 49, 315 – 335, https://doi.org/10.1016/S0169-8095(98)00083-0, 1998.